

6th CIRP Conference on Surface Integrity

Numerical and experimental investigation on the residual stresses generated by scanning induction hardening

Maialen Areitioaurtena^a, Unai Segurajauregi^a, Martin Fisk^{b,c}, Mario J. Cabello^a, Eneko Ukar^d^a*Ikerlan Technology Research Centre, Basque Research and Technology Alliance (BRTA), Paseo J.M. Arizmendiarieta 2, 20500 Arrasate-Mondragon, Spain.*^b*Department of Materials Science and Applied Mathematics, Malmö University, Malmö, Sweden.*^c*Division of Solid Mechanics, Lund University, P.O. Box 118, SE-221 00 Lund, Sweden.*^d*Department of Mechanical Engineering, University of the Basque Country, Alameda Urquijo s/n, 48013 Bilbao, Spain.** Corresponding author. Tel.: +34 943 71 24 00. E-mail address: mareitioaurtena@ikerlan.es

Abstract

Induction hardening is widely used in the industry as a surface heat treatment that improves the surface and the subsurface hardness of components greatly. The hardened case, which usually is a few mm, highly impacts the surface and structural integrity of the component. In this work, we simulate the scanning induction hardening process by means of finite element modeling. The computed hardness, microstructure, and residual stress profile are compared with experimentally measured data using several surface and subsurface characterization techniques. A very good agreement is found between the simulated and experimentally measured residual stresses, which were characterized by the incremental hole drilling technique.

© 2022 The Authors. Published by Elsevier B.V.

This is an open access article under the CC BY-NC-ND license (<https://creativecommons.org/licenses/by-nc-nd/4.0>)

Peer review under the responsibility of the scientific committee of the 6th CIRP CSI 2022

Keywords: Induction hardening; residual stresses; numerical simulation

1. Introduction

The induction hardening process is a surface hardening technique that is becoming more popular in the industry as a result of the benefits it provides over conventional heat treatments. It is most commonly utilized on critical components that are subjected to high loads and high pressure contacts, which require an elevated surface hardness. Although the industry's interest in this heat treatment is growing, the definition of the most important process parameters is typically limited to the technicians' know-how and previous experiences, which increases associated costs and time-to-market because process design is typically done through trial-and-error procedures. Because of the various interactions between physical fields, the simulation of induction hardening is highly complicated and computationally expensive. Generally speaking, the usage of the induction hardening process in complex industrial components is hampered by the absence of numerical models capable of predicting the results of this process. Thus, it is easy to conclude numerical simulation is key in the development of the induction hardening process in the modern industry.

As a result of a typical induction hardening process, a layer of hard martensite is achieved in the surface zone. Immediately after the hardened case, a transition zone between the hardened and unhardened zones is found, in which considerable microstructure and hardness gradients are observed. The core of the components, which has not exceeded austenitization temperatures, have a lower hardness from the initial microstructure. When it comes to residual stresses, the hardened case generally has compressive residual stresses, while the unhardened core has tensile stresses, especially in the transition area [1]. In Figure 1 (a) a typical hardness and residual stress distribution is shown. The final properties of a induction hardened component are highly dependent on the applied process, since induction hardening is very sensitive to the input parameters [2–4].

When scanning induction hardening is applied, there is a relative movement between the workpiece and the inductor, which generally produces a homogeneous hardened case in the treated region. Scanning induction hardening is typically applied to large size bearings and tooth-by-tooth hardening of gears, as well as cylindrical components such as camshafts, crankshafts and shafts. In Figure 1 (b) a photograph of a scanning induction hardening process applied to cylinders is shown. In Figure 1 (c)

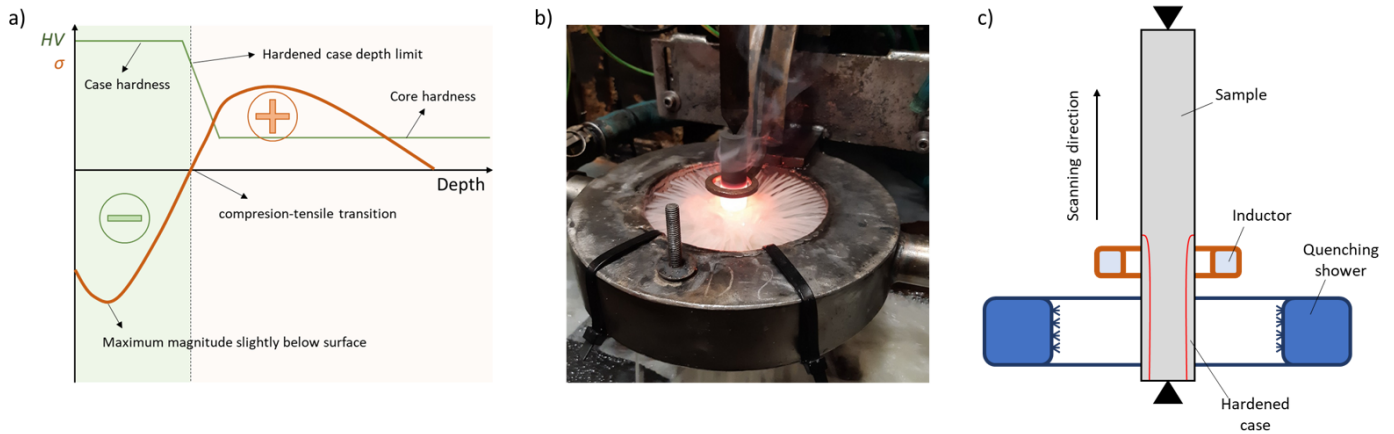


Fig. 1. a) Typical residual stress profile achieved by induction hardening, b) a scanning induction hardening process c) graphical representation and main components in a scanning induction hardening setup.

a graphical representation indicates the most important components of a scanning induction hardening system.

In [5] the authors developed an induction hardening simulation model using the ABAQUS and ANSYS softwares, each solving part of the process. The convection coefficient used by the authors was $10,000 \text{ W/m}^2\text{K}$, which resulted in superficial residual stresses that varied between -200 MPa and 300 MPa depending on the measurement position. However, no experimental validation is shown for the sub-surface residual stresses, where the residual stresses vary from -300 MPa in the hardened case and up to 600 MPa in the transition area. In [6] a simulation strategy using several commercial softwares was presented. The authors simulated the induction hardening process using Flux2D® and DANTE® where the electromagnetic-thermal coupling and the thermo-mechanical coupling were solved, respectively. The database provided by DANTE® was used to generate the TTT diagrams and dilatometry curves required for the analysis. After solving the induction heating and cooling problem in Flux2D®, the temperature history was transferred into DANTE® to calculate microstructural phases, hardness and residual stress profiles. The authors investigated the impact of different convection coefficients in the generation of residual stresses in the workpiece, concluding that a faster quenching generates higher magnitude stresses. Unfortunately, the authors carried out a numerical analysis without experimental validation.

The experimental measurement of residual stresses in induction hardened components is typically carried out by means of X-ray diffraction and the Incremental Hole Drilling (IHD) technique. The measurements carried out with the X-ray diffraction technique are usually limited to a depth of a few μm unless electro polishing techniques are used to measure higher depths, which makes this technique more suitable for surface hardening techniques such as shot peening or carburizing [7, 8]. For induction hardening the IHD technique is more typically used. The IHD method is based on placing a gauge rosette in the specimen's surface and drilling a hole in the center, measuring the deformations associated with the relaxation of residual stresses in that area. According to the ASTM Standard E837-13a, in

cases of non-homogeneous residual stresses, as in the case of induction hardening, the measuring depth is 1 mm .

In this work, the numerical simulation of the scanning induction hardening process in low alloy 42CrMo4 cylinders is addressed. The numerical model allows the prediction of microstructure, hardness and residual stress profiles achieved with the process. The influence of the quenching conditions into the material characteristics after induction hardening is discussed. Experimental tests are carried out, where two different quenching media are used. The obtained residual stresses are measured using the IHD technique and the results are compared.

2. Modeling scanning induction hardening

Induction hardening is composed of two different phases that, even though they occur simultaneously in a scanning process, can be differentiated numerically speaking: induction heating and quenching. During induction heating, the numerical simulation must be able to solve the electromagnetic diffusion equation (1) to be able to compute the Joule heating that occurs inside the workpiece.

$$\sigma \frac{\partial \mathbf{A}}{\partial t} - \nabla \left(\frac{1}{\mu} \nabla \mathbf{A} \right) = \mathbf{J}_s \quad (1)$$

The electromagnetic diffusion equation (1) is the result of the combination of the well-known Maxwell's electromagnetic equations. In FEM solvers, the source current (\mathbf{J}_s) is considered time-harmonic. Thus, equation (1) is solved in a steady-state computation using the harmonic approximation, where the magnetic permeability of the material (μ) is often linearized for non-linear ferromagnetic materials.

Once the heat generation is computed, the heat conduction equation (2) is solved. This equation allows the calculation of the temperature distribution inside the workpiece, which depends on the internal heat generation caused by the Joule heat-

ing (\dot{Q}) and the thermal properties of the material (specific heat capacity and thermal conductivity).

$$\rho c_p \frac{\partial T}{\partial t} - \nabla (\kappa \nabla T) = \dot{Q} \quad (2)$$

Details on how to solve the electromagnetic-thermal coupled problem, as well as the equations to calculate the microstructural transformations and hardness are given in references [9] and [10]. The models by Avrami (also known as JMAK) and Koistinen and Marburger (see [9]) are implemented to account for austenite formation and its transformation into martensite. The hardness is evaluated from the chemical composition of the steel alloy and the cooling rate according to the models presented in [9]. A linear rule of mixture is used to calculate the total hardness at each computation node, depending on the existing phase fraction and its specific hardness.

2.1. Residual stress

In this work the residual stress generation is focused on the macroscopic scale. The total strain rate tensor in the macroscopic scale governs the material behavior when it is subjected to temperature changes and phase transformations [11]. The total strain rate tensor is defined as

$$\dot{\varepsilon}_{ij} = \dot{\varepsilon}_{ij}^{\text{el}} + \dot{\varepsilon}_{ij}^{\text{th}} + \dot{\varepsilon}_{ij}^{\text{tr}} + \dot{\varepsilon}_{ij}^{\text{pl}} + \dot{\varepsilon}_{ij}^{\text{tp}} \quad (3)$$

where $\dot{\varepsilon}_{ij}^{\text{el}}$ is the elastic strain, $\dot{\varepsilon}_{ij}^{\text{th}}$ the thermal strain, $\dot{\varepsilon}_{ij}^{\text{tr}}$ the transformation strain, $\dot{\varepsilon}_{ij}^{\text{pl}}$ the conventional plastic strain, $\dot{\varepsilon}_{ij}^{\text{tp}}$ the transformation induced plasticity (TRIP strain).

In the following each strain contribution is discussed [11].

Elastic strain The elastic strain is the deformation that is fully recovered upon removal of the applied load and follows Hooke's law. In a material that is under phase transformation, the material properties are typically calculated using a linear rule of mixture.

Thermal strain The thermal strains appear due to the dilatation and contraction of the material with temperature change. In induction hardened specimens, the great temperature gradients that are achieved in the material typically cause large thermal strains. A dilatometric curve allows the evaluation of the Coefficient of Thermal Expansion for each microstructural phase.

Transformation strain Upon phase transformation, the crystal rearrangement causes a local volumetric change. This volumetric change can be measured in a dilatometric test. However, it is common to combine thermal and transformation strains ($\varepsilon_{ij}^{\text{tt}} = \varepsilon_{ij}^{\text{th}} + \varepsilon_{ij}^{\text{tr}}$) through an equivalent CTE approach such as in [12]. The equivalent CTEs, which account for thermal and transformation strains, can be obtained from dilatometric curves. Generally, two different CTEs are obtained (heating

and cooling), depending on the existing phases and their transformations.

Conventional plastic strain When the phase-specific yield stress is exceeded, the materials begin to behave plastically, where the deformation is not recovered upon removal of the load. In this work, a bilinear isotropic hardening model is used to account for the plastic behavior of the material.

Transformation Induced Plasticity (TRIP) The TRIP strain is a plastic strain that is observed during the volumetric change of microstructural phases under stresses. This occurs at stress levels below the yield strength of the materials as a result of a plastic accommodation of the weaker phase because of the volume change in the neighboring crystals. Details on how to account for TRIP strain are given in the works by Leblond [13]. The TRIP strain is calculated as

$$\varepsilon_{ij}^{\text{tp}} = \frac{3}{2} K \sigma'_{ij} g(f) \frac{df}{dt} \quad (4)$$

The function $g(f)$, which has many expressions that can be found in the literature, has been expressed as $g(f) = f(2 - f)$ in this work [14], where f indicates phase fraction. The parameter K is typically $K = 42 \times 10^{-6} \text{ MPa}^{-1}$ for 42CrMo4 [15].

The presented equations were implemented in ANSYS via subroutines or User Programmable Features (UPFs). The subroutines were written in Fortran and an ANSYS Custom Executable was compiled in order to perform simulations using the developed subroutine structure.

3. Experimental tests

The induction hardening setup can be seen in Figure 1 (b) while the most important components are represented in Figure 1 (c). 42CrMo4 cylinders with 20 mm diameter and 75 mm length were scan hardened using the same induction heating parameters for both samples. However, two different cooling conditions were experimentally studied. Samples A were fast quenched with a 4 % polymer concentration and samples B were quenched slower with a 12 % polymer concentration, although the quenching rate was high enough to obtain a 100 % martensitic phase in the surface area. The used polymer was AQUACOL VSL-FF, which is a water dilutable polymer. As a result, different hardness and residual stress profiles were obtained, which can be shown in Figure 2. In Figure 2 (b) a transversal cross-section is shown, where the hardened case can be observed after etching. The microstructure of the transition area marked in (b) can be observed in Figure 2 (a) with a magnification of 100x.

Hardness values were measured using a Vickers micro-indenter and the residual stresses were measured by the Incremental Hole Drilling method with a type-B gauge rosette. Axial and tangential residual stresses were measured. In the following, axial residual stresses are compared in a depth of 1 mm from the surface. Three measurements were performed for each

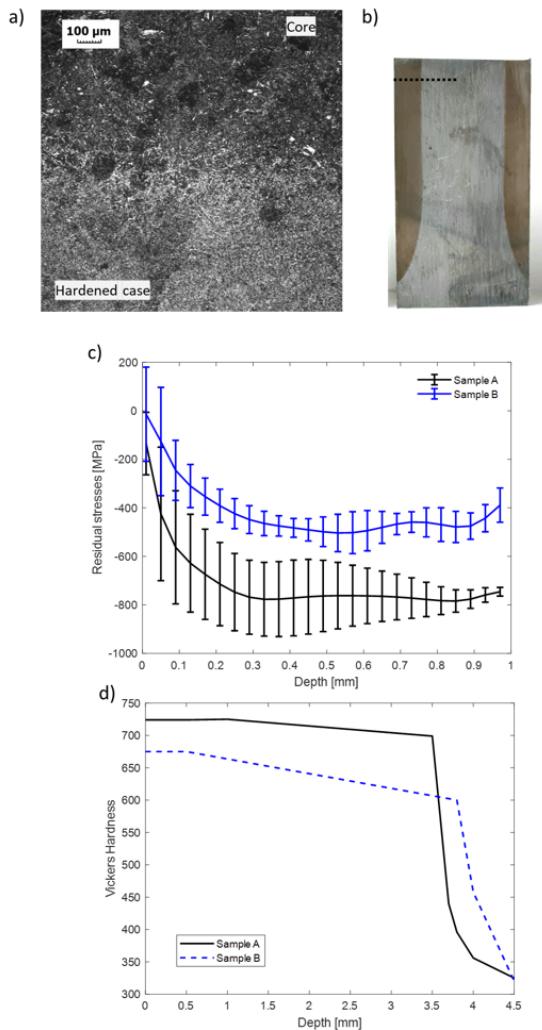


Fig. 2. Experimentally obtained microstructure in the transition area after etching (a) and etched hardened case in a transversal cross-section (b), where the position of hardness measurements and location of microstructural observations are shown, residual stress profiles (c) and hardness (d) for samples A and B.

sample type. In Figure 2 (c) mean value and standard deviation are shown for each sample type. It has been previously documented that there is certain uncertainty in the near-surface region when using the Hole Drilling method, which might be caused by the surface roughness, the geometry of the workpieces or the setting of the reference surface for the measurements [16]. In Figure 2 (d) hardness values are shown, where it is possible to observe that the depth of the hardened case is slightly lower than 4 mm.

For sample A, the obtained hardness was approximately 725–700 HV in the hardened case with high compressive residual stresses in the surface area (–800 MPa). For sample B, a lower hardness was obtained (between 675 HV and 600 HV) with compressive residual stresses of lower magnitude (–400 MPa).

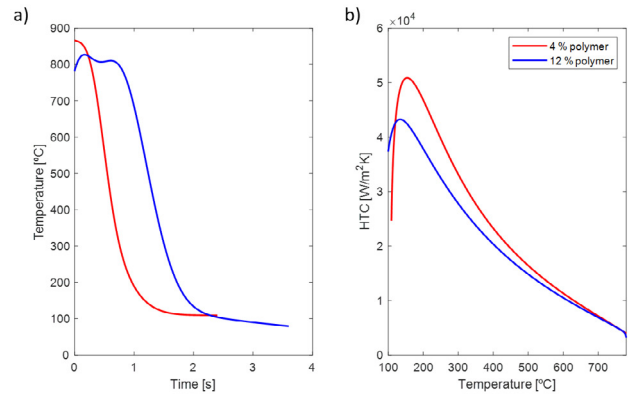


Fig. 3. Experimentally measured temperatures (a) and calculated temperature-dependent convection coefficients (b).

4. Induction hardening simulations

An axisimetric model was constructed using 14k linear elements. The process parameters were kept constant in the simulations with a current intensity of 2616 A (RMS) with a frequency of 17 kHz. The scanning speed was set to 9 mm/s. The convection coefficients were estimated from experimentally measured temperatures using the inverse temperature gradient procedure presented in [17]. The temperatures were measured using spot-welded type-K thermocouples. Figure 3 shows the experimentally measured temperatures and the calculated temperature-dependent convection coefficients used for the simulations.

Additionally, in order to numerically study the influence of the quenching conditions into the generation of residual stresses during scanning induction hardening, five different convection coefficients have been studied: 25,000 W/m²K, 20,000 W/m²K, 15,000 W/m²K, 10,000 W/m²K, 5,000 W/m²K. For the sake of simplicity, these have been considered constant.

5. Results and discussion

In Figure 4 (a) the experimentally measured residual stresses are compared to the numerically obtained stresses for samples A and B. Both the experimentally and numerically obtained residual stresses are compressive in the transformed region, which is in agreement with experimental data reported in the literature. This is the result of the non-diffusive microstructural transformation, where the carbon trapped in the crystal structures generates a carbon-saturated and highly-strained Body Center Tetragonal crystal, which produces high macro-stresses in the transformed region. In the Figure, it is possible to observe that the residual stresses have been accurately predicted between 0.3 mm and 1 mm, while the stresses in the initial increments of the experimental measurement differ from the numerically obtained results. However, as it has been previously stated, the measurement in the initial increments of the Hole Drilling method are related to certain uncertainties, which are

increased when cylindrical surfaces with high convex curvatures are evaluated. Thus, it is reasonable to ignore the initial measurement increments for the correlation study between the experimental and numerical results.

The obtained martensitic case depth is shown in Figure 4 (b), where it is possible to observe that the workpiece is not hardened at the starting position (low end) as there has not been enough time to reach austenitization temperatures. After the initial transient stage austenite is achieved in a homogeneous depth until the inductor reaches the upper edge of the billet, where the magnetic field concentrates and austenite is obtained in a higher depth.

In Figure 4 (c) different residual stress profiles are shown along the maximum and minimum values, which have been obtained using different convection coefficients. Although the depth of the hardened case is very similar for all cases, the obtained maximum and minimum residual stresses differ.

5.1. Influence of quenching conditions into residual stress generation

From the experimental and numerical results, it is possible to conclude that a faster cooling rate provided by a higher convection coefficient gives more compressive residual stresses in the surface of the specimen, which generally improves component performance, especially if the component is subjected to fatigue failure. However, higher tensile residual stresses are also obtained in the transition region between the hardened and non-hardened areas when a fast cooling is applied, which can be observed in the numerically obtained residual stress maps in Figure 4 (c). Unfortunately, the Incremental Hole Drilling technique used in this work to measure residual stresses did not allow to perform measurements in the transition region, which is located in a depth of 3.5 to 4 mm.

Thus, the results indicate that a higher quenching rate will generate a larger residual stress gradients, which might affect component performance and overall process result. The high tensile stresses that appear in the transition region when an aggressive quenching is applied are associated with quench cracking, a phenomenon that might occur during quenching if improper quenching media is selected or if the components have geometrical or internal characteristics that favor crack opening when internal stresses build up during the cooling process. Regarding the hardness values, the experimentally measured hardness profiles demonstrate that a higher quenching rate produces a harder microstructure, as the hardness of the different microstructures depends on the cooling rate at high temperatures.

6. Conclusions

A numerical model to include phase transformations, hardness and residual stress generation during scanning induction hardening has been developed and implemented in ANSYS. The model has been used to evaluate the impact of the quenching rate in the generation of residual stresses, concluding that a faster quenching generates stresses of higher magnitude, both

compressive in the surface area and tensile in the untreated core. Experimentally measured residual stress profiles show that the tendency predicted by the numerical results is maintained, where the fastest cooling rate produces residual stresses of higher magnitude (800 MPa, compressive) than the slower quenched specimen (400 MPa, compressive). This fact becomes especially important for industrial cases where cooling conditions might be variable due to polymer degradation and cleanliness, as the samples might exhibit a similar case depth that fits the specifications but with different residual stress profiles, which affect in-service performance. Additionally, the great stress gradient produced by an aggressive quenching rate might be associated to a component failure due to quench cracking, as the internal stresses built up during the process might be too large and produce a crack initiation and opening. In summary, selecting an appropriate quenching medium is therefore determinant for avoiding quench cracking and obtaining a material with required characteristics.

Acknowledgements

Ikerlan's research has been supported by CDTI, depending by Ministerio de Ciencia e Innovación, through the AYUDAS CERVERA PARA CENTROS TECNOLÓGICOS 2019 program, project MIRAGED with expedient number CER-20190001. This research centre is certificated as CENTRO DE EXCELENCIA CERVERA.

References

- [1] C. Simsir, Modeling and Simulation of Steel Heat Treatment — Prediction of Microstructure, Distortion, Residual Stresses, and Cracking, ASM International, Materials Park, OH 4 (B) (2014) 1–2.
- [2] V. Rudnev, D. Loveless, R. L. Cook, Handbook of induction heating, no. August, Taylor & Francis, Boca Raton, FL, 2017.
- [3] G. Krauss, Steels - Processing, Structure and Performance, 2nd Edition, ASM International, Ohio, 2015.
- [4] ASM International, ASM Handbook - 4. Heat treating, Vol. 4, 1991. doi:10.1016/S0026-0576(03)90166-8.
- [5] X. Wang, Q. Meng, Z. Wang, J. Gan, Y. Yang, X. Qin, K. Gao, H. Zhong, M. Cheng, X. Gan, Prediction of the surface characteristic of 42CrMo after spot continual induction hardening based on a novel co-simulation method, Surface and Coatings Technology 357 (October 2018) (2019) 252–266. doi:10.1016/j.surfcoat.2018.09.088.
- [6] Z. Li, B. L. Ferguson, V. Nemkov, R. Goldstein, J. Jackowski, G. Fett, Stress Generation in an Axle Shaft during Induction Hardening, Journal of Materials Engineering and Performance 23 (12) (2014) 4170–4180. doi:10.1007/s11665-014-1196-0.
- [7] Los Alamos National Laboratory, Slitting: Comparison with other residual stress measurement methods, Tech. rep. (2007).
- [8] J. Holmberg, A. Steuwer, A. Stormvinter, H. Kristoffersen, M. Haakana, J. Berglund, Residual stress state in an induction hardened steel bar determined by synchrotron- and neutron diffraction compared to results from lab-XRD, Materials Science and Engineering A 667 (2016) 199–207. doi:10.1016/j.msea.2016.04.075.
- [9] M. Areitioaurtena, U. Segurajaregi, I. Urresti, M. Fisk, E. Ukar, M. Fisk, Predicting the induction hardened case in 42CrMo4 cylinders, Procedia CIRP 87 (2020) 545–550. doi:10.1016/j.procir.2020.02.034.
- [10] M. Areitioaurtena, U. Segurajaregi, V. Akujarvi, M. Fisk, I. Urresti, E. Ukar, A semi-analytical coupled simulation approach for induction heat-

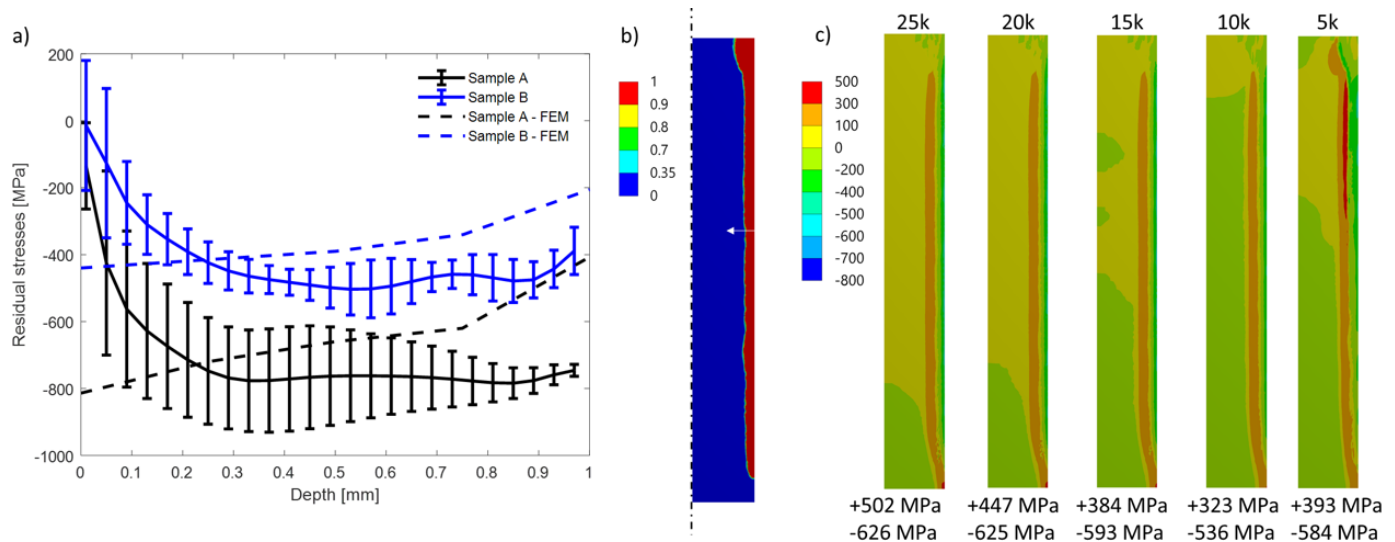


Fig. 4. Simulated and experimentally measured residual stresses (a) and martensite case depth (b) and residual stress maps with different quenching conditions (c).

ing, *Advanced Modeling and Simulation in Engineering Sciences* 8 (14). doi:10.1186/s40323-021-00199-0.

- [11] S. Sjöström, The Calculation of Residual Stress, Measurement of Residual and Applied Stress Using Neutron Diffraction (1992) 67.91.
- [12] L. Pan, W. He, B. Gu, Effect of crystallographic orientation on quenching stress during martensitic phase transformation of carbon steel plate, *Journal of Wuhan University of Technology-Mater. Sci. Ed.* 32 (5) (2017) 1213–1219. doi:10.1007/s11595-017-1733-4.
- [13] J. Leblond, G. Mottet, J. Devaux, A theoretical and numerical approach to the plastic behaviour of steels during phase transformations—I. Derivation of general relations, *Journal of the Mechanics and Physics of Solids* 34 (4) (1986) 395–409. doi:10.1016/0022-5096(86)90009-8.
- [14] D. Kaiser, J. Damon, F. Mühl, B. de Graaff, D. Kiefer, S. Dietrich, V. Schulze, Experimental investigation and finite-element modeling of the short-time induction quench-and-temper process of AISI 4140, *Journal of Materials Processing Technology* 279. doi:10.1016/j.jmatprotec.2019.116485.
- [15] J. Rohde, A. Jeppsson, Literature review of heat treatment simulations with respect to phase transformation, residual stresses and distortion, *Scandinavian Journal of Metallurgy* 29 (2) (2000) 47–62. doi:10.1034/j.1600-0692.2000.d01-6.x.
- [16] J. P. Nobre, C. Polese, S. N. van Staden, Incremental Hole Drilling Residual Stress Measurement in Thin Aluminum Alloy Plates Subjected to Laser Shock Peening, *Experimental Mechanics* 60 (4) (2020) 553–564. doi:10.1007/s11340-020-00586-5.
- [17] B. Liščić, T. Filetin, Measurement of Quenching Intensity, Calculation of Heat Transfer Coefficient and Global Database of Liquid Quenchants, *Materials Engineering - Materiálové inžinierstvo (MEMI)* 19 (2) (2012) 52–63–63.